

Single-shot impulsive stimulated Brillouin microscopy by tailored ultrashort pulses

David Krause^{1,2,a,*}, Leon Liebig¹, John Boehm¹, Nektarios Koukourakis^{1,2,a}, and Juergen W. Czarske^{1,2,3,4} 

¹ Laboratory of Measurement and Sensor System Technique, TU Dresden, Helmholtzstrasse 18, 01069 Dresden, Germany

² Competence Center for Biomedical Computational Laser Systems (BIOLAS), TU Dresden, 01069 Dresden, Germany

³ Cluster of Excellence Physics of Life, TU Dresden, 01069 Dresden, Germany

⁴ School of Science, Faculty Physics, TU Dresden, 01069 Dresden, Germany

Received 19 November 2024 / Accepted 20 January 2025

Abstract. Brillouin microscopy has become an important tool for investigating the mechanical properties of tissue. The recently developed Impulsive Stimulated Brillouin Scattering (ISBS) promises a label-free, non-invasive measurements of viscoelastic properties of transparent samples and offers the potential for a high temporal resolution. However, the spatial resolution of ISBS is currently limited. Increasing the spatial resolution of ISBS leads to an increase in the energy density of the pump beams, which requires a balancing of the excitation parameters to stay below the phototoxic threshold. This paper focuses on the influences of different excitation parameters on the spatial, temporal, and spectral resolution and their optimal values. Combined with the adoption of a noise suppressing window function, a measurement rate of 20 $\mu\text{s}/\text{pixel}$ in hydrogel is achieved, which is promising for fast 3D imaging. The presented advanced impulsive stimulated Brillouin microscopy can be applied for fast tissue elastography toward disease studies.

Keywords: Single-shot, Exponential window, Interface effects.

1 Introduction

The study of mechanical properties of biological material provides important insights into its biological function [1, 2] and can characterize the pathological states of tissue [3]. Consequently, mechanical mapping of tissue by medical imaging is a rapidly developing field that has emerged as a valuable tool in biomedical research and is already used in clinical practice as organ-level diagnostic assistance tool for various diseases such as prostate cancer [4, 5], liver fibrosis [6], and breast lesions [7]. Many techniques have been developed, such as ultrasound elastography [8] and atomic force microscopy (AFM) [9]. However, the acquisition of mechanical properties at sub-cellular resolution has long posed significant challenges, primarily due to the reliance of traditional techniques on direct physical contact or their insufficient cellular resolution. Optical elastography on the other hand offer various advantages over classical methods, being non-invasive, contactless, label-free, and can provide cellular or even sub-cellular resolution [3].

An emerging optical elastography technique is Brillouin Microscopy (BM) which is based on the interaction of light

(photons) with an acoustic wave (phonons) [10–15] and has become a highly appreciated technique for studying condensed matter systems [16–18]. The spontaneous BM (SpBM) offers high spatial resolution, but is based on the interaction of photons with spontaneous occurring thermal phonons leading to long integration times due to the low signal-to-noise ratio (SNR) and therefore making the application of SpBM in clinics difficult. Despite these challenges line measurements at acquisition times in the range of 100–200 ms, which effectively equates to 1 ms/pixel, have been accomplished [19, 20].

The active stimulation of phonons, instead of the resonant spontaneous scattering of thermally generated phonons, can lead to an efficiency that is orders of magnitude higher and thus to faster imaging. Stimulated Brillouin Scattering (SBS) utilizes two slightly detuned continuous-wave (cw) lasers for phonon excitation (pump and probe technique) [21–25]. The higher SNR leads to lower integration times and measurements rates of ~ 20 ms/pixel were achieved [23], however, the wavelength must be scanned to measure the entire spectrum, which outweighs the advantage of the lower integration times. Impulsive Stimulated Brillouin Scattering (ISBS) holds promise for achieving measurement rates in the MHz range, owing to the signal generation through the interaction of ultra-short laser pulses

^aThese authors contributed equally to this work

* Corresponding author: david.krause@tu-dresden.de

[26–31], taking advantage of the nonlinear nature of Brillouin light scattering. ISBS makes full use of the higher SNR to decrease the temporal resolution in contrast to SBS, because the signal is evaluated in the time domain, removing the need for a wavelength scan. The higher temporal resolution of ISBS, facilitated by the interaction of two pump pulses and a probe beam, can significantly reduce measurement duration's. This advancement is crucial for both rapid imaging in clinical applications and fundamental research, such as studying morphogenesis at the organism level during gastrulation in *Drosophila* [20]. The measurement of elastic properties also plays an important role in organoids. In the optogenetics of transgenic organoids, elasticity measurements are desirable to learn about the transfer functions from light stimulus to mechanical reaction [32].

The interference fringes formed by two intersecting laser pulses create phonons at the intersection point, where the probe photons are inelastically scattered. The stiffness of the material is linked to the Doppler frequency shift of the inelastically scattered photons. A investigation was performed on the influences of the pulse and probe parameters on the SNR and it was concluded that the choice of high pulse energies offers the greatest leverage [33]. However, when focusing sharper to increase the spatial resolution, the increasing excitation energy density needs to be taken into account to avoid phototoxic effects. Recently Li et al. [29] performed a similar study, where they investigated the influence of the probe beam parameters and acquisition time. In this paper, we expand the investigation on optimizing the ISBS excitation process, which requires balancing the influence of excitation parameters, like the repetition rate on the spatial and spectral resolution. The temporal resolution of ISBS is increased by incorporating the exponential window function [34] into the signal analysis process.

2 Materials and methods

ISBS microscopy relies on creating a transient density grating using an ultra-short pulsed laser and probing it through Bragg diffraction with a continuous wave (cw) laser. The pulsed laser beam is divided into two coherent beams via a diffraction grating. The interference of these coherent laser beams forms an interference fringe system [35], with fringe spacing d determined by the excitation beam's wavelength λ_{pump} and the half-crossing angle ϕ_{pump} :

$$d = \frac{\lambda_{\text{pump}}}{2 \sin \phi_{\text{pump}}}. \quad (1)$$

The impulsive excitation of a standing acoustic wave is induced by either electrostrictive or thermal coupling of the laser pulse to the material within the measurement volume. This density variation also alters the refractive index. Consequently, a portion of the probe beam is diffracted at a temporally varying refractive index grating under the Bragg condition, resulting in intensity modulation. For electrostrictive excitation, the expected modulation frequency is $f_2 = 2c_s/d$, where c_s is the sound velocity in the sample. If the signal is thermally excited, the expected frequency is

$f_1 = c_s/d$ [36]. Electrostriction exerts a force on matter along the gradient of the absolute electric field strength [37], causing displacement of matter toward regions of high light intensity. Thermal excitation heats the matter in regions of higher light intensity, leading to impulsive expansion. The resulting temporal changes in matter are governed by thermodynamic material equations. The single diffracted probe beam can either be detected alone or in a heterodyne fashion [38]. In the heterodyne scenario, the probe beam is reflected by the standing wave and another coherent part of the probe beam are superimposed on the photodetector. This additional part can be intentionally generated or arise inadvertently in the setup. For purely electrostrictive excitation with heterodyne detection, the expected frequency is f_1 . Both frequencies can be utilized to measure sound velocity and, consequently, deduce mechanical properties.

The experimental setup is depicted in Figure 1. It is essentially the same architecture that was used in our previous work [33], with the only difference being that we now use pump laser with $\lambda_{\text{pump}} = 1035$ nm, while the probe beam is still at $\lambda_{\text{probe}} = 895$ nm (DL100 Toptica Photonics). The pump laser is a Coherent Monaco, which offers a tunable pulse-length, repetition-rate and pulse energy. The probe beam diffraction orders propagate between the diffraction orders of the grating for the pump laser. Both pump and probe beams are focused on the diffraction grating (GT) and the ± 1 diffraction orders are focused with the 4f-system to create the measurement volume. The choice of lenses is essential for the ISBS process. The -1 diffraction order of the probe beam is used to adjust the optical setup, but is later blocked to only detect the Brillouin scattered light. After the measurement volume, a long-pass filter removes the remaining pump light in the optical pathway and the Brillouin scattered probe beam is focused on an avalanche photodiode (APD). The oscilloscope (Tektronix MSO64B) reads out the time signal from the APD and sends it to a PC for analysis.

3 Signal strength

The primary objective of this work is to find a balance between multiple experimental parameters that optimize the SNR of ISBS, resulting in faster measurement rates while simultaneously maintaining a high spatial and spectral resolution.

3.1 Excitation parameters

With the configuration depicted in Figure 1, we studied an excitation cross-section diameter of 40 μm and a matched diameter for the probe beam. The fringe spacing in the excitation volume is 3 μm . The measurements were all conducted on a water filled cuvette with 500 μm axial extent and lateral dimensions of 5 mm. We use signal strength, simply defined as the fitted peak height in the Fourier spectrum, as a measure.

At first the signal strength was measured for different pulse length and different pulse energies at a fixed repetition

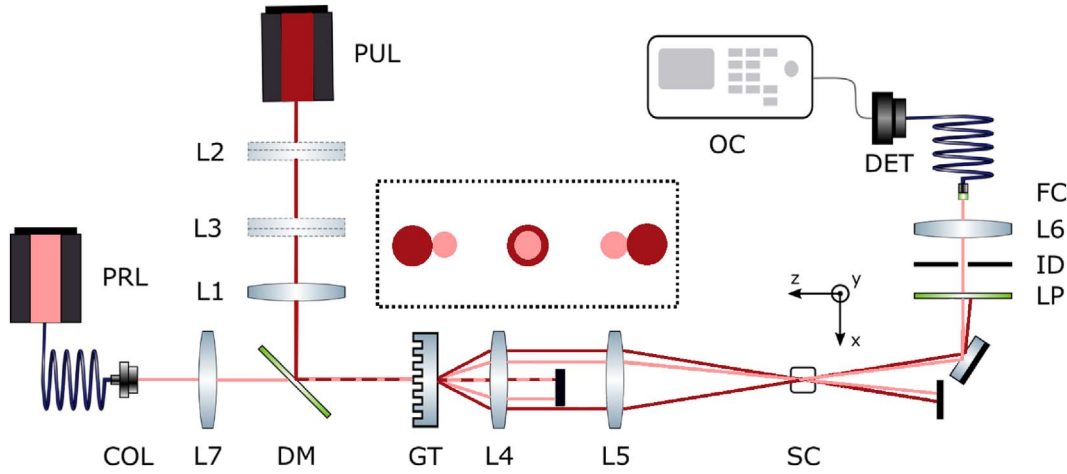


Figure 1. ISBS microscope setup: PUL excitation laser (1035 nm, Coherent Monaco); PRL probe laser (895 nm, DL100 Toptica Photonics); DM dichroic mirror (DMLP650 Thorlabs); COL collimator; L1 to L6 achromatic lenses (AC245-Series Thorlabs); GT grating (custom, grating constant 8 μm); SC sample container (Fused Quartz Cuvettes Thorlabs); ID iris diaphragm; LP long-pass (FEL0850 Thorlabs); DET detector (APD, Femto Berlin); OC oscilloscope.

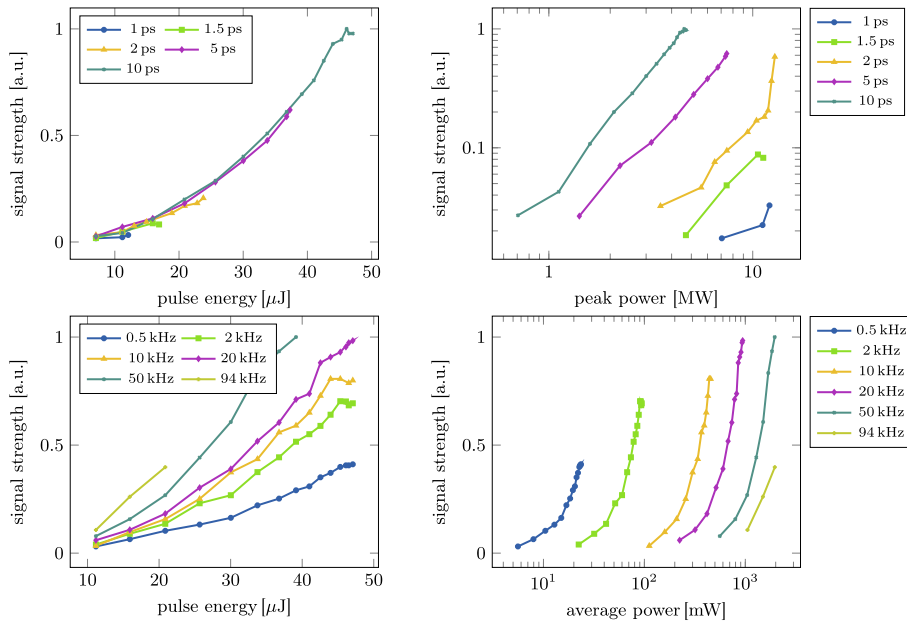


Figure 2. The dependence of the normalized signal strength in water on (top left) different pulse energies and pulse lengths, (top right) different peak powers and pulse lengths, (bottom left) different pulse energies and repetition rates and (bottom right) different average powers and repetition rates. For the top row the repetition rate was set to 1 kHz and in the bottom row the pulse length was kept constant at 10 ps for all measurements. Arbitrary unit (a.u.).

rate of $k = 1$ kHz and averaging over $N = 1000$ measurements. The signal strength increases non-linear with the pulse energy for different pulse length (Fig. 2, top left), making it advantageous to work with high energy pulses, while the pulse length does not seem to influence the signal strength, as the slope for all pulse length is the same. However, the resulting peak power is higher for shorter pulse length and we observed a fluctuation of the peak frequency at around 10 MW for water. We attribute this effect to phototoxicity induced by high peak powers, and

consequently, the use of longer pulse length is advantageous for maintaining sample integrity and ensuring reliable measurements. The peak power \hat{P} can be calculated by $\hat{P} = E_p/t_p$, with E_p and t_p being the pulse energy and pulse length respectively. As plotted in the top right of Figure 2, a good parameter choice for a high SNR is a high pulse energy while keeping the pulse length long to reduce the peak power. However, the pulse length must be much shorter than the acoustic period for the excitation to be considered impulsive. It should be noted, that all quantitative limits

derived in this paper are dependent on the sample and on the sensitivity of the experimental setup. Most importantly the behavior will be different for different pump wavelengths.

In the subsequent analysis, we employ pulse duration's of $t_p = 10$ ps, while changing both the repetition rate and the pulse energy to alter the average power $\bar{P} = E_p \cdot k$. Both the pulse energy and the repetition rate increase the signal strength, illustrated in the bottom left in [Figure 2](#), which suggests picking the highest value for each possible. But also for the average power a threshold is observed, above which the peak frequency started to fluctuate with an added drift of the peak frequency, which can be attributed to induction of heat. The repetition rate and pulse energy would be selected in such a way that the average power remains below the specified threshold, thus the determination of this threshold for a given sample is important. The trade-offs between choosing a high pulse energy or high repetition rate will be discussed in the next section.

3.2 Exponential window

So far we have looked at how the SNR can be improved by increasing the signal strength with the optimal excitation parameter choice. Another valid option to improve the SNR is to lower the noise of the signal. In the frequency analysis of signals with the fast Fourier transform (FFT), the signal is commonly windowed [39] (each time point is weighted with a weighting function, the *window*) to reduce the spectral leakage, but can also help to reduce the noise. For decaying signals the exponential window is a widely utilized option, because it minimizes the attenuation at its strongest point (the beginning), while ensuring a gradual decline to zero at the end. These characteristics can help improve the SNR [34] and make the adoption of this window for the exponentially damped ISBS signal an ideal choice.

Although the signal is altered through the multiplication with the exponential window, these changes can be calibrated for. Assuming the following intensity signal

$$I(t) = \sin(2\pi ft)e^{-\alpha_1 t} \quad (2)$$

with $I(t)$, f , and α_1 being the light intensity at the detector, frequency, and the damping coefficient of the signal, respectively. When this signal is then multiplied with the exponential window the resulting signal will be

$$I_w(t) = \sin(2\pi ft)e^{-\alpha_1 t} e^{-\alpha_2 t} \quad (3)$$

$$= \sin(2\pi ft)e^{-(\alpha_1 + \alpha_2)t} \quad (4)$$

with $I_w(t)$, α_2 being the windowed intensity signal and decay coefficient of the exponential window respectively. The linewidth of the peak in the frequency spectrum will now correspond to the sum of both decay coefficients $\Delta_f = \sqrt{3}(\alpha_1 + \alpha_2)/\pi$ [40]. But as α_2 is known a priori the calculation of the damping coefficient simply becomes $\alpha_1 = \pi\Delta_f/\sqrt{3} - \alpha_2$.

To show the advantages of the exponential window in low SNR situations, simulations were carried out with different SNRs. For each SNR 100 signals are evaluated,

allowing to estimate the variance of each method. The exponential window has the lowest variance both for the damping coefficient and the Brillouin frequency for low SNRs ([Fig. 3](#), stays stable even for SNRs of -12 dB). In this low SNR situations it is challenging to determine the end of the signal, potentially leading to the inclusion of noise at the end of the time-domain signal. This makes the exponential window especially effective in situations with a low SNR or when the signal decays quickly because of large damping coefficients.

To experimentally verify that the exponential window can increase the temporal resolution while accurately measuring the viscoelastic properties at low SNRs, measurements on ethanol were performed. A reference for the Brillouin frequency and linewidth of ethanol was created by averaging 10,000 measurements (corresponds to 1000 ms and SNR of 6 dB), which were taken with a pulse energy of 41 μ J. The averaged signal was evaluated with the FFT to obtain both the Brillouin frequency of 443.75 MHz and the linewidth 17.80 MHz. Afterwards measurements are taken at a reduced pulse energy with 20 averages, corresponding to only 0.4 ms/measurement. The resulting Brillouin frequency of 440.25 MHz deviates by 0.79% from the reference value even though the SNR is only -12.1 dB. The linewidth can also be determined accurately using the exponential window 17.22 MHz deviates only by 3.26% compared to the reference. The exponential window thus demonstrates the ability to measure both Brillouin frequency and linewidth, indicating that using the exponential window requires a SNR as low as -12.1 dB, thereby substantially reducing the required number of averages and optical power.

4 Spatial and temporal resolution trade-off

Thus far we investigated the optimal excitation parameters for a fixed spatial resolution. Now we want to expand on the considerations when changing the spatial resolution and how this affects the temporal resolution. The achievable temporal resolution is limited by the usable repetition rate and the required number of averages to obtain an adequate SNR. Although the SNR increases with \sqrt{N} through averaging, the measurement time also increases proportional to N . Therefore, it is crucial to optimize the SNR of a single measurement to minimize the required averages. Therefore, it is optimal to select the highest possible pulse energy and pick a repetition rate accordingly, which together stay below the average power threshold. The relationship between spatial and temporal resolution is constrained by the maximum allowable average power density of the sample. Once this limit is reached for a given spatial resolution, further improvement in spatial resolution necessitates a reduction in pulse energy to maintain the sample's integrity. This reduction in pulse energy results in a lower SNR, which must be compensated for by increasing the number of averages, thereby decreasing the temporal resolution. Consequently, enhancing spatial resolution beyond this point involves a trade-off with temporal resolution. The optimal balance between these parameters

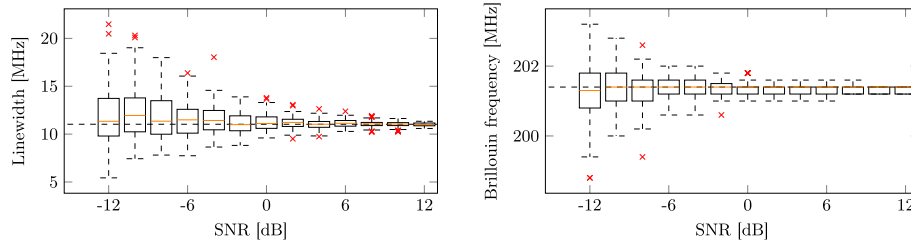


Figure 3. The measured linewidth (left) and peak frequency (right) of 100 simulated signals and evaluated with the exponential window. The orange line, the upper and lower edge of the boxes correspond to the median value, the 25th and 75th percentiles respectively. The dashed line from each box extends to the minimum or maximum non-outlier value inside the distribution. The red x's indicate outliers, which are more than 1.5 the interquartile range away from the first or third quartile. The horizontal dashed line indicates the ground truth.

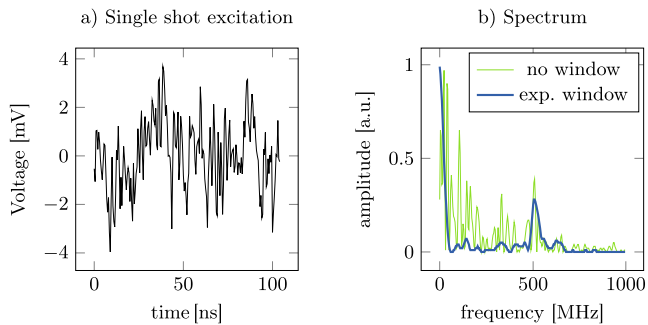


Figure 4. a) Time signal of a single-shot measurement from water and b) the corresponding frequency spectrum once evaluated without and with exponential window.

depends on the specific requirements of the experiment or application.

To illustrate these principles in practice, we conducted experiments at a spatial resolution of $40\ \mu\text{m}$. With pulse energies of $E_p = 35\ \mu\text{J}$ and a pulse repetition rate of $50\ \text{kHz}$ single-shot measurements were possible without using the exponential window for data evaluation. Consecutive measurements varied less than 0.3% of the peak frequency, which we define here as adequate measurement quality. However, the average power is very close to the maximum applicable dose. In order to not to impair the sample a $20\ \mu\text{J}$ pulse energy and $50\ \text{kHz}$ repetition rate were chosen as parameters. Now only the data evaluation with the exponential windows leads to single-shot measurement (Fig. 4) and it is possible to acquire the peak frequency and linewidth. There is still a peak present at the frequency of hydrogel in the spectrum when no window is used, but the SNR is too low for a reliable result.

As a simple example we applied stage-scanning to record 2D images of a hydrogel cube, freshly located in water with a coarse spatial resolution of $100\ \mu\text{m}$ (Fig. 5). Hydrogel mostly contains water and to increase the image contrast it was dried before it was placed inside of the water. The hydrogel and the water frequencies can be clearly distinguished, see Figure 5 on the right. While the exact frequency difference is hard to estimate, the frequency difference of $50\ \text{MHz}$ seems reasonable, as the dried hydrogel cube is stiffer and one would expect a higher Brillouin

frequency. With the measurement point rate of $50\ \text{kHz}$ the theoretical frame rate for this $24\ \text{pixel}$ image is $0.48\ \text{ms}$ corresponding to a pixel measurement rate of $20\ \text{s/pixel}$, which is around two orders of magnitudes faster than current then SpBM techniques.

5 Spatial and spectral resolution trade-off

Increasing the spatial resolution effects also the spectral resolution. When the spatial resolution is increased, the angle of the two pump beams increases and thus the number of fringes inside the excitation volume increases as well (Eq. (1) leading to a higher Brillouin frequency). More critically, this leads to a shorter signal duration in time. The excited phonons naturally propagate outside the excitation volume, a process that occurs more rapidly in smaller excitation volumes. For instance, with a $40\ \mu\text{m}$ excitation diameter, the signal in water persists for approximately $40\ \text{ns}$. For a $40\ \mu\text{m}$ excitation diameter, the signal in water lasts approximately $40\ \text{ns}$. According to the Cramer-Rao lower bound (CRLB), this short signal duration fundamentally limits the obtainable spectral resolution. Specifically, the CRLB indicates that the minimum variance of any unbiased estimator of the frequency is inversely proportional to the signal duration [41]. The spectral resolution should not be confused with the resolution of the Fourier sampling, which can be enhanced by zero padding and improves the peak determination accuracy. Hence, a small measurement volume is mainly usable in homogeneous media, where one frequency is present. If two materials are located in the measurement volume and the spectral resolution is not high enough to distinguish the corresponding two peaks, the measurement will be distorted by a shifted peak position, as the two peaks will merge into one peak with broader bandwidth.

Recently O'Connor et al. [42] proposed a line excitation, which extends the time signal, because phonons are excited over a larger area and will propagate into the probe beam with a delay. The line excitation was realized by employing a cylindrical lens instead of the spherical lens L1 in Figure 1 to focus the pump beam on the grating. The probe beam keeps its symmetric profile, which in our case has a full width at half maximum (FWHM) of approximately

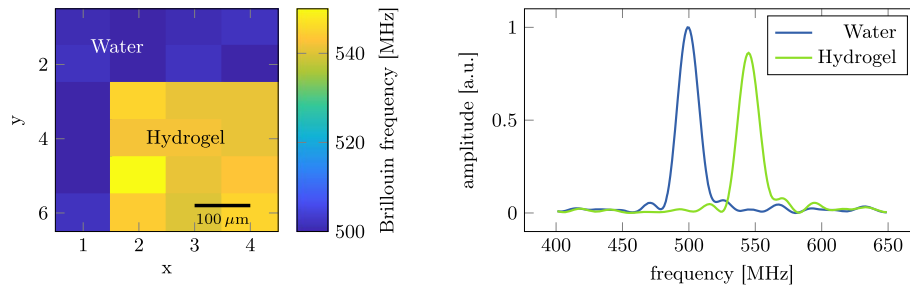


Figure 5. (left) A low spatial resolution image (4×6 pixels) of a hydrogel cube embedded in water using the Brillouin frequency as contrast. (right) Example spectra of water and hydrogel from two pixels of the left image.

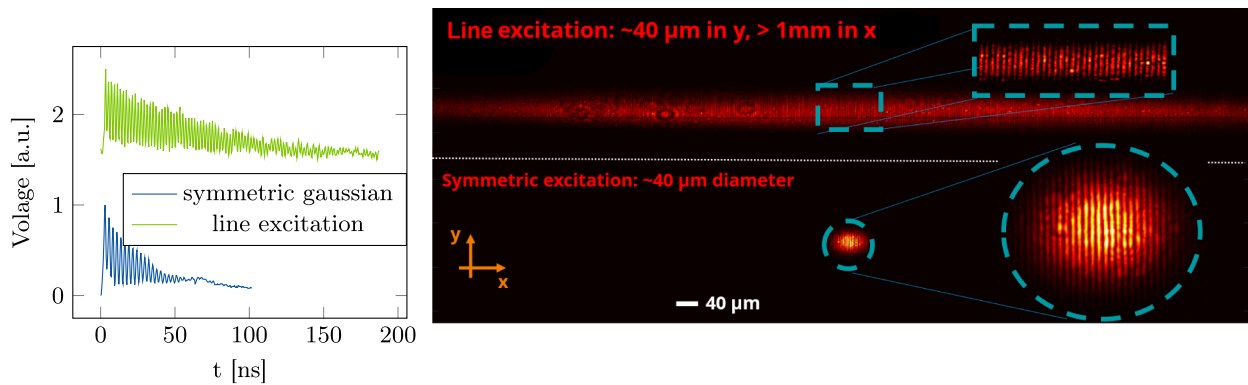


Figure 6. (left) Time signals for a symmetric gaussian and line excitation (offset added for clarity). (right) Images of the two excitation profiles.

$40 \mu\text{m}$ (Fig. 6). Additionally, the line excitation also allows for the usage of higher pulse energies, as the line excitation spreads the deposited energy over a large area. However, the increase in spectral resolution is achieved at the expense of lower spatial resolution in the x -direction.

This trade-off between spectral and spatial resolution becomes particularly interesting when considering material interfaces, where the unique properties of phonon propagation can be observed. If the excitation cross section overlaps at an interface of two different materials, it will create phonons in both materials with the same wavelength, because the same interference grating is imprinted in both materials. However, due to different sound velocities in the materials the phonons will have different frequencies. When phonons transmit through an interface they change their wavelength, but their frequency will stay constant. This frequency will be detected when the phonon passes through the probe area (Fig. 7a). The detection of the frequency depends on the transmission efficiency of phonons through the interface and the attenuation of the phonons, rendering it therefore sample dependent. If the probe beam is in close proximity to the interface, the intersection between the probe and the interference grating under an angle also leads to the detection of both frequencies (Fig. 7b). The probe beam gets reflected from the grating in both materials. The strength of this volumetric effect depends on the intersection angle and the axial extent of the interference fringes.

To investigate phonon transmission across interfaces, we conducted an experiment using a line excitation profile on a wet hydrogel cube immersed in water. We selected a wet hydrogel cube for its relatively smooth surface compared to its dried counterpart, minimizing potential scattering effects at the interface. To analyze the signal behavior at varying distances from the interface, we performed a lateral scan of the sample, systematically altering the position at which the probe beam entered the sample. Figure 8 presents the spectra obtained from this horizontal scan, revealing the evolution of the Brillouin signal as a function of distance from the hydrogel-water interface. Starting far from the interface, the ISBS signal shows only the frequency of hydrogel $f = 500 \text{ MHz}$. The Brillouin frequency of this cube differs from the one used in Figure 4, because the cube was made out of a softer hydrogel. Moving closer to the interface, the excited phonons in water transmit through the water/hydrogel interface and propagate through the probe area, leading to the detection of the water frequency (493 MHz). The position, where the two peaks are of equal height, corresponds to the interface position, because the line excitation excites an equal amount of phonons in both media. In our case this would be at the position $x = 90 \mu\text{m}$. In the vicinity of the interface, both the volume effect and the crosstalk effect superimpose, whereas in the outer regions only the crosstalk effect exists. The data suggest that the crosstalk in that sample is limited to $\sim 90 \mu\text{m}$ around the interface, because at $x = 190 \mu\text{m}$ only the water

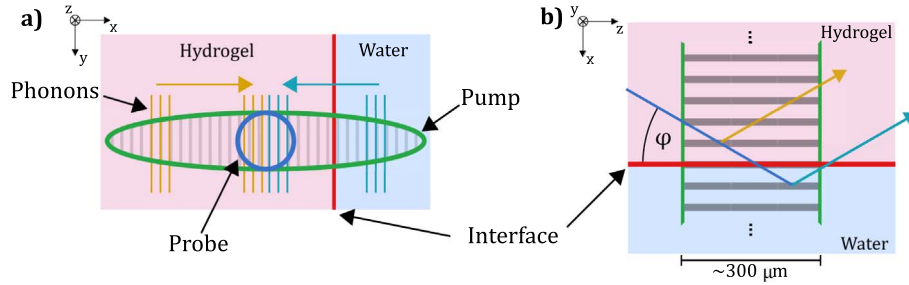


Figure 7. a) Schematic of an line excitation in x -direction, which excites phonons in water and hydrogel, which after some time will reach the probe beam. When the water phonons transmit through the interface, they will propagate through the probe beam. b) Schematic of the volumetric effect, where due to the angle φ the probe beam is reflected both in water and hydrogel, even though the center of the probe beam is in hydrogel.

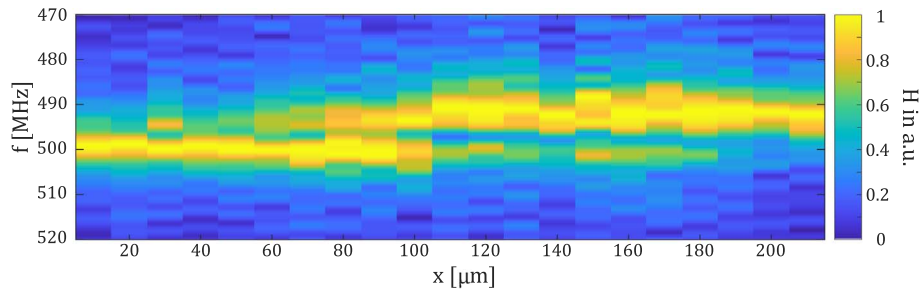


Figure 8. Individually normalized spectra at different x positions when scanning a line excitation over a hydrogel-water interface, starting in hydrogel, showing the slope of the frequency change.

frequency is detected. This indicates a strong attenuation of the acoustic waves or a weak coupling between the two materials. The two different materials can be clearly distinguished after $\sim 180 \mu\text{m}$, corresponding to the effective spatial resolution along the x -axis.

6 Discussion

The noise suppression capability of the exponential window comes at the cost of a reduced spectral resolution of the system. The reduction in spectral resolution depends on the decay coefficient of the exponential and can be tuned, resulting in a spectral resolution which is up to 3 times larger compared to the analysis without a window. By tuning the decay coefficient you trade off a higher spectral resolution against the noise suppression capability and spectral leakage. Small decay coefficients offer a higher spectral resolution, but increased spectral leakage, while using larger decay coefficients improves noise suppression but at a lower spectral resolution. Thus, according to the SNR of the signal the decay coefficient should be picked. For low SNR signals a high decay coefficient is beneficial due to the noise suppression, but for higher SNR signals a lower decay coefficient can be viable.

Crucial parameters for measurements are the maximum allowable light dose and the sensitivity of the detection. These parameters limit the usable peak and average powers of the pump laser and thus the SNR and the achievable measurement rates. It is generally desirable to approach

the imposed limits of the sample in order to obtain the best possible SNR. For long-time observations, the pulse energy should be reduced because at a repetition rate of 50 kHz and a pulse energy of 20 μJ the induced heating changes the speed of sound inside the sample.

For a fixed spectral resolution the speed of sound resolution could be further improved by decreasing the interference fringe distance d . This changes the expected frequency f_e following the equation for excitation $f_e = v_u/d$, with v_u being the ultrasonic velocity. This is a linear equation which grows steeper with decreasing interference fringe spacing, see Figure 9. Following the equation of the fringe spacing $d = \lambda_{\text{pump}}/(2\sin\theta)$, with θ being half the intersection angle of the pump beams, d is at its smallest value when the angle between the pump beams is increased to 180° , leading to counter propagating pump beams. When two materials exhibit similar v_u 's, it is easier to distinguish both materials with small fringe distances because a small change in v_u leads to a larger difference in frequency compared to bigger fringe distances, which in theory is easier to detect.

The advantages of the steeper slope are two-fold regarding the spatial and speed of sound resolution respectively. Under the assumption that the phonon attenuation is approximately constant for the frequency range used, the signal duration for a given spatial resolution is constant. This means that the spectral resolution is also constant, resulting in a higher speed of sound resolution. There exists a relationship of the phonon frequency to the attenuation of phonons in solids [43], but it has to be investigated on how it affects the signal duration in liquid or biological samples.

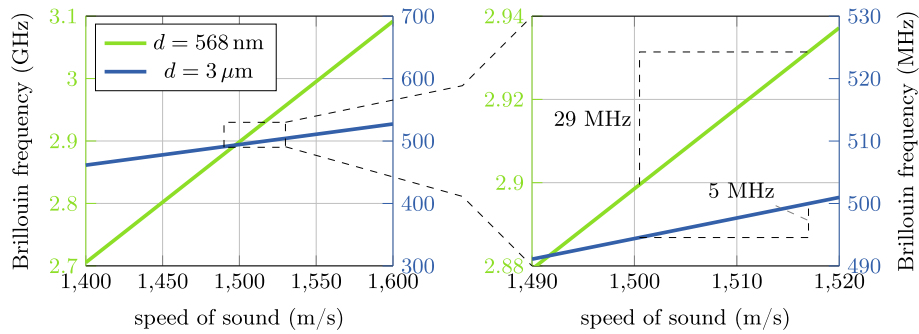


Figure 9. Relationship of the speed of sound to the Brillouin frequency for a grating period of $d = 3 \mu\text{m}$ and $d = 568 \text{ nm}$.

If on the other hand the improved speed of sound resolution is not required, the smaller fringe spacing has the benefit of requiring shorter time signals to achieve the same resolution in the speed of sound. In the case of a hydrogel cube embedded in water, which have a difference in the speed of sound of $\sim 17 \text{ m/s}$ (1.1 %), the frequency difference between the two materials in the crossed beam setup would be 7 MHz and in the counter propagating setup would result in 29 MHz (Fig. 9 on the right). Measurement of such a difference would require a $\sim 140 \text{ ns}$ long signal in the crossed beams setup, compared to only 35 ns in the counter propagating setup. This would allow for a higher spatial resolution, because the time signal shortens with decreasing focus size. For a given speed of sound resolution, the counter propagating setup thus enables a higher spatial resolution. But the approach with the counter propagating pump is harder to align than the setup depicted in Figure 1, where the probe and pump beam automatically fulfill the Bragg condition if focused correctly at the grating.

When modifying the pump beam profile for a better spectral resolution and SNR, it is crucial to bear in mind the impact on the spatial resolution. Altering the initial pump profile by expanding it along the x -axis using a cylindrical lens leads to enhancements in spectral resolution and spatial resolution along the y -axis. However, it also results in a notable decrease in spatial resolution along the x -axis. This decline is mostly influenced by the crosstalk of the different media and strongly sample dependent. The transmission efficiency of the interface and the attenuation of the material affect the amount of crosstalk. In our case this leads to a spatial resolution of $\sim 180 \mu\text{m}$ in x -direction.

The final challenge to enable fast imaging is to find an alternative to stage scanning, which limits the frame rate at the moment. The hurdle is, that during scanning of the probe beam the Bragg condition needs to be fulfilled. Thus, the beams incident to the grating should just shift laterally orthogonal to the grating, which can be realized with a 2D galvo scanning system.

7 Conclusion

In this paper, we investigated the influences of the excitation parameters of ISBS on the SNR and how this effects the temporal and spatial resolution. High temporal resolution is important to achieve high-throughput measurements.

The pulse energy and average power are the most significant excitation parameters for increasing the signal strength. Using longer pulses length lowers the peak power of the pulse, which increases the maximum allowed pulse energy. Through the introduction of a line shaped pump profile in the x -direction the spectral resolution got improved by a factor of ~ 4 with probe beam size of $\sim 40 \times 40 \mu\text{m}^2$. The probe beam size is currently limited by the focal length of the used optics, but can be improved further to $\sim 14 \times 14 \mu\text{m}^2$ [29]. By also spreading the pulse energy over a larger area, higher pulse energies are possible, which positively influence the SNR. The here presented temporal resolution of $20 \mu\text{s}/\text{pixel}$ of ISBS is two orders of magnitude higher compared to SpBM and one order of magnitude higher than the previous best temporal resolution reported for ISBS [29]. In combination with a detector array, line measurements of 100 pixel would result in an effective measurement rate of $200 \text{ ns}/\text{pixel}$, which would enable real-time imaging.

Acknowledgments

The authors would like to thank Anna Taubenberger (Biotechnology Center, TU Dresden) for providing hydrogel samples.

Funding

Deutsche Forschungsgemeinschaft (Cz55/44-1).

Conflicts of interest

The authors declare no conflicts of interest.

Data availability statement

Data underlying the results presented in this paper are not publicly available at this time but may be obtained from the authors upon reasonable request.

Author contribution statement

All authors made significant contributions to this work.

References

- Kennedy BF, Wijesinghe P, Sampson DD, The emergence of optical elastography in biomedicine, *Nat. Photonics* 11, 4 (2017). <https://doi.org/10.1038/nphoton.2017.6>.

- 2 Koukourakis N, et al. Investigation of human organoid retina with digital holographic transmission matrix measurements, *Light Adv. Manuf.* **3**, 2 (2022). <https://doi.org/10.37188/lam.2022.023>.
- 3 Learthrapun N, Adie SG, Recent advances in optical elastography and emerging opportunities in the basic sciences and translational medicine [Invited], *Biomed. Opt. Express* **14**, 1 (2022). <https://doi.org/10.1364/boe.468932>.
- 4 Correas JM, et al. Ultrasound elastography of the prostate: State of the art, *Diagn. Interv. Imaging* **94**, 5 (2013). <https://doi.org/10.1016/j.diii.2013.01.017>.
- 5 Pallwein L, et al. Prostate cancer diagnosis: value of real-time elastography, *Abdom. Imaging* **33**, 6 (2008). <https://doi.org/10.1007/s00261-007-9345-7>.
- 6 Jaffer OS, et al. Is ultrasound elastography of the liver ready to replace biopsy? A critical review of the current techniques, *Ultrasound* **20**, 1 (2012). <https://doi.org/10.1258/ult.2011.011043>.
- 7 Itoh A, et al. Breast disease: clinical application of US, *Radiology* **239**, 2 (2006). <https://doi.org/10.1148/radiol.2391041676>.
- 8 Sigrist RMS, et al. Ultrasound elastography: review of techniques and clinical applications, *Theranostics* **7**, 5 (2017). <https://doi.org/10.7150/thno.18650>.
- 9 Gautier HOB, et al. Atomic force microscopy-based force measurements on animal cells and tissues, *Methods Cell Biol.* **125**, 211 (2015). <https://doi.org/10.1016/bs.mcb.2014.10.005>.
- 10 Antonacci G, et al. Recent progress and current opinions in Brillouin microscopy for life science applications, *Biophys. Rev.* **12**, 3 (2020). <https://doi.org/10.1007/s12551-020-00701-9>.
- 11 Raimund S, et al. Mechanical mapping of spinal cord growth and repair in living zebrafish larvae by Brillouin imaging, *Biophys. J.* **115**, 5 (2018). <https://doi.org/10.1016/j.bpj.2018.07.027>.
- 12 Czarske J, Heterodyne detection technique using stimulated Brillouin scattering and a multimode laser, *Opt. Lett.* **19**, 19 (1994). <https://doi.org/10.1364/ol.19.001589>.
- 13 Coker ZN, et al. Brillouin microscopy monitors rapid responses in subcellular compartments, *PhotonIX* **5**, 1 (2024). <https://doi.org/10.1186/s43074-024-00123-w>.
- 14 Moeckel C, et al. Estimation of the mass density of biological matter from refractive index measurements, *bioRxiv* (2023). <https://doi.org/10.1101/2023.12.05.569868>.
- 15 Pruidze P, et al. Brillouin scattering spectroscopy for studying human anatomy: Towards in situ mechanical characterization of soft tissue, *J. Eur. Opt. Soc., Rapid Publ.* **19**, 31 (2023). <https://doi.org/10.1051/jeos/2023028>.
- 16 Dil JG, Brillouin scattering in condensed matter, *Rep. Prog. Phys.* **45**, 3 (1982). <https://doi.org/10.1088/0034-4885/45/3/002>.
- 17 Hua Z, et al. Non-destructive and distributed measurement of optical fiber diameter with nanometer resolution based on coherent forward stimulated Brillouin scattering, *Light Adv. Manuf.* **2**, 4 (2021). <https://doi.org/10.37188/lam.2021.025>.
- 18 Alunni Cardinali M, et al. Brillouin scattering from biomedical samples: the challenge of heterogeneity, *J. Phys. Photon.* **6**, 035009 (2024). <https://doi.org/10.1088/2515-7647/ad4cc7>.
- 19 Zhang J, et al. Rapid biomechanical imaging at low irradiation level via dual line-scanning Brillouin microscopy, *Nat. Methods* **20**, 677 (2023). <https://doi.org/10.1038/s41592-023-01816-z>.
- 20 Bevilacqua C, et al. High-resolution line-scan Brillouin microscopy for live imaging of mechanical properties during embryo development, *Nat. Methods* **20**, 755 (2023). <https://doi.org/10.1038/s41592-023-01822-1>.
- 21 Remer I, Bilenca A, Background-free Brillouin spectroscopy in scattering media at 780 nm via stimulated Brillouin scattering, *Opt. Lett.* **41**, 5 (2016). <https://doi.org/10.1364/ol.41.000926>.
- 22 Remer I, et al. High-sensitivity and high-specificity biomechanical imaging by stimulated Brillouin scattering microscopy, *Nat. Methods* **17**, 9 (2020). <https://doi.org/10.1038/s41592-020-0882-0>.
- 23 Yang F, et al. Pulsed stimulated Brillouin microscopy enables high-sensitivity mechanical imaging of live and fragile biological specimens, *Nat. Methods* **1**, 9 (2023). <https://doi.org/10.1038/s41592-023-02054-z>.
- 24 Ballmann CW, et al. Stimulated Brillouin scattering microscopic imaging, *Sci. Rep.* **5**, 1 (2015). <https://doi.org/10.1038/srep18139>.
- 25 Li T, et al. Quantum-enhanced stimulated Brillouin scattering spectroscopy and imaging, *Optica* **9**, 8 (2022). <https://doi.org/10.1364/optica.467635>.
- 26 Ballmann CW, et al. Impulsive Brillouin microscopy, *Optica* **4**, 124 (2017). <https://doi.org/10.1364/OPTICA.4.000124>.
- 27 Krug B, Koukourakis N, Czarske J, Impulsive stimulated Brillouin microscopy for non-contact, fast mechanical investigations of hydrogels, *Opt. Express* **27**, 19 (2019). <https://doi.org/10.1364/oe.27.026910>.
- 28 Le T, et al. Speed of sound measurement and mapping in transparent materials by impulsive stimulated Brillouin microscopy, *J. Phys. Photon.* **6**, 035004 (2024). <https://doi.org/10.1088/2515-7647/ad46a8>.
- 29 Li J, et al. High-speed impulsive stimulated Brillouin microscopy, *Photon. Res.* **12**, 730 (2023). <https://doi.org/10.1364/prj.509922>.
- 30 Meng Z, Petrov GI, Yakovlev VV, Flow cytometry using Brillouin imaging and sensing via time-resolved optical (BISTRO) measurements, *Analyst* **140**, 21 (2015). <https://doi.org/10.1039/c5an01700a>.
- 31 Ballmann CW, Meng Z, Yakovlev VV, Nonlinear Brillouin spectroscopy: what makes it a better tool for biological viscoelastic measurements, *Biomed. Opt. Express* **10**, 4 (2019). <https://doi.org/10.1364/boe.10.001750>.
- 32 Schmieder F, et al. Tracking connectivity maps in human stem cell-derived neuronal networks by holographic optogenetics, *Life Sci. Alliance* **5**, 7 (2022). <https://doi.org/10.26508/lsa.202101268>.
- 33 Krug B, et al. Nonlinear microscopy using impulsive stimulated Brillouin scattering for high-speed elastography, *Opt. Express* **30**, 4748 (2022). <https://doi.org/10.1364/OE.449980>.
- 34 Fladung W, Rost R, Application and correction of the exponential window for frequency response functions, *Mech. Syst. Signal Process.* **11**, 23 (1997). <https://doi.org/10.1006/mssp.1996.0084>.
- 35 Günther P, et al. Distance measurement technique using tilted interference fringe systems and receiving optic matching, *Opt. Lett.* **37**, 22 (2012). <https://doi.org/10.1364/ol.37.004702>.
- 36 Schlamp S, et al. Accuracy and uncertainty of single-shot, nonresonant laser-induced thermal acoustics, *Appl. Opt.* **39**, 30 (2000). <https://doi.org/10.1364/ao.39.005477>.

- 37 Boyd RW, *Nonlinear optics*, 4th edn (Academic Press, 2020). <https://doi.org/10.1016/C2015-0-05510-1>.
- 38 Maznev AA, Nelson KA, Rogers JA, Optical heterodyne detection of laser-induced gratings, *Opt. Lett.* **23**, 16 (1998). <https://doi.org/10.1364/ol.23.001319>.
- 39 Prabhu KMM, *Window functions and their applications in signal processing* (Taylor & Francis, 2014). <https://doi.org/10.1201/9781315216386>.
- 40 Li J, et al. Sensitive impulsive stimulated Brillouin spectroscopy by an adaptive noise-suppression Matrix Pencil, *Opt. Express* **30**, 29598 (2022). <https://doi.org/10.1364/OE.465106>.
- 41 Czarske J, Statistical frequency measuring error of the quadrature demodulation technique for noisy single-tone pulse signals, *Meas. Sci. Technol.* **12**, 5 (2001). <https://doi.org/10.1088/0957-0233/12/5/307>.
- 42 O'Connor SP, et al. Spectral resolution enhancement for impulsive stimulated Brillouin spectroscopy by expanding pump beam geometry, *Opt. Express* **31**, 14604 (2023). <https://doi.org/10.1364/OE.487131>.
- 43 Zhu TC, Maris HJ, Tauc J, Attenuation of longitudinal-acoustic phonons in amorphous SiO₂ at frequencies up to 440 GHz, *Phys. Rev. B* **44**, 9 (1991). <https://doi.org/10.1103/physrevb.44.4281>.